Journal of Fluids and Structures 113 (2022) 103672

Contents lists available at ScienceDirect

Journal of Fluids and Structures

journal homepage: www.elsevier.com/locate/jfs

Experimental study of tornado-like loading on rectangular prisms

Zhuo Tang [a], Delong Zuo [a,*], Darryl James [a], Yuzuru Eguchi [b], Yasuo Hattori [b]

[a] National Wind Institute, Texas Tech University, 1009 Canton Ave., Lubbock, TX, USA
[b] Fluid Dynamics Sector, Civil Engineering Research Laboratory, Central Research Institute of Electric Power Industry, Abiko 1646, Abiko-shi, Chiba-ken, Japan

ARTICLE INFO

Article history:
Received 29 July 2020
Received in revised form 8 April 2022
Accepted 6 July 2022
Available online 22 July 2022

Keywords:
Tornado
Wind loading
Rectangular prisms

ABSTRACT

To study the interaction between bluff bodies and tornado-like flow, two rectangular prisms of different depth to height ratios were tested in a two-celled tornado-like vortex generated by a Ward-type tornado simulator. The measurements are interpreted to reveal the characteristics of the mean and dynamic components of the tornado-like loading in the context of the velocity and static pressure fields of the tornado-like flow as well as the dependences of these characteristics on the radial location and the clearance of the prisms in the simulated vortex. The effects of the difference in the depth to height ratios of the prisms on the tornado-like loading are also evaluated. In addition to the fundamental understanding of tornado-like loading on bluff bodies, the study produces an experimental dataset that can serve as benchmarks for the validation and calibration of numerical methods used for the study of tornado-like loading on structures.

1. Introduction

As tornadoes continue to rank among the most destructive natural hazards, studies of tornadic winds and their effects on the built environment have gained much momentum in recent decades. Many field campaigns have been conducted to investigate the genesis of tornadoes (e.g., Bluestein et al., 2007; Houser et al., 2015), the structures of the wind and pressure fields inside tornadoes (e.g., Karstens et al., 2010; Kosiba and Wurman, 2010, 2013), and the damages that tornadoes have caused (e.g., Lombardo et al., 2015). Meanwhile, laboratory and numerical simulations have also seen significant advancements. Many tornado simulators of various designs and sizes have been built to facilitate experiments in simulated tornado-like vortices (e.g., Haan et al., 2008; Refan and Hangan, 2018; Sabareesh et al., 2012; Tang et al., 2018a; Wang et al., 2017), and an increasing number of numerical investigations based on Computation Fluid Dynamics (CFD) have been conducted, many of which were for replicating physical experiments in tornado simulators (e.g., Gairola and Bitsuamlak, 2019; Liu and Ishihara, 2015; Liu et al., 2018; Natarajan and Hangan, 2012).

To date, most studies of tornado-like loading on bluff bodies, including structures, have utilized laboratory and numerical approaches, primarily due to the challenges in directly measuring the loading on full-scale bluff bodies by tornadoes. Jischke and Light (1984) conducted one of the earliest comprehensive experiments in a tornado simulator to study the tornado-like loading on structures. The data from the experiments suggested that, due to the swirling of tornadic winds, tornado-like loading on a rectangular prism can be significantly different from the loading by straight-line winds and that tornado-like loading depends on the orientation and location of the model relative to the core of the tornado-like

* Corresponding author.
E-mail address: delong.zuo@ttu.edu (D. Zuo).

https://doi.org/10.1016/j.jfluidstructs.2022.103672
0889-9746/

vortex. Subsequently, many more experiments have been performed in tornado simulators to investigate various aspects of tornado-like loading on structural models of simple shapes. Some of these studies focused on the tornado-like loading on the external surfaces of the bluff bodies, highlighting the significant differences between tornado-like loading and the loading by boundary-layer-type winds (e.g., Mishra et al., 2008) and the effects of the location of the bluff body and ground roughness on the peak and the mean pressures acting on different regions of the building envelope (Sabareesh et al., 2012). Some other studies focused on the internal pressure of bluff bodies of simple shapes (e.g., Letchford et al., 2015; Rajasekharan et al., 2013; Sabareesh et al., 2013) subjected to tornado-like vortices. The effects of the location of the model relative to the simulated vortex, the size of the dominant opening and the amount of background leakage in the model envelop, and the ground roughness on the internal pressure were investigated. In the study by Letchford et al. (2015), internal pressure measurement was compared with the prediction by a Helmholtz resonator model (e.g., Holmes, 1979; Kopp et al., 2008) with the measured external pressure as the input. The characteristics of the internal pressure caused by the tornado-like vortex was also compared with those of the internal pressure in the same bluff body when it is exposed to boundary layer flow in a wind tunnel.

In addition to the studies of tornado-like loading on simple shapes, experiments have also been conducted to study tornado-like loading on models of more complex shapes. Haan et al. (2010) tested a model of a gable-roofed building in a number of different tornado-like vortices generated by the tornado simulator at Iowa State University. The study suggested that tornado-like loading on the building can be much larger than the corresponding wind loading specified by design provisions for boundary layer type winds. It is also revealed that increasing the translation speed of the tornado-like vortex usually results in a reduction of the loading on the model. In a subsequent study, the external pressures measured in these experiments were used as the inputs in multiple discharge equations to estimate the internal pressures of the model, and tornado-like loading due to both external and the internal pressures were compared to the loading on a similar gable-roofed building model tested in a boundary layer wind tunnel (Roueche et al., 2020). Using the same tornado simulator, Thampi et al. (2011) tested a model of a realistic gable-roofed building in a vortex that was simulated to represent a full-scale tornado. Both the external pressures and the internal pressure were measured, and the measurements from the experiments were used along with a finite-element model of the building to evaluate the failure of the prototype structure. In a study that is not related to buildings, Cao et al. (2015) measured the pressure acting on a cooling tower model by tornado-like vortices, revealing that tornado-like loading on the cooling tower also can be significantly different from the loading on the tower by boundary-layer-type winds.

While many laboratory simulations have been used to study tornado-like loading of structures, only a few studies based on Computational Fluid Dynamics (CFD) have been performed for this purpose. Selvam and Millet (2003, 2005) used the technique of large eddy simulation (LES) to model the interaction between a Rankine-combined vortex model of tornadic winds and a low-rise building. The results of the simulation were used to investigate the differences between tornado-like loading and loading by boundary-layer-type winds on different building components. Liu et al. (2018) used LES to numerically evaluate tornado-like loading on a cooling tower, and the differences between the tornado-like loading and loading by boundary-layer-type winds are also evaluated. In particular, this study suggested that the tornado-like loading is primarily affected by the sub-vortex when the tower is close to the inner core of the vortex and vortex-shedding off the tower when the tower is in the outer regions of the vortex.

While previous experimental and numerical studies have significantly contributed to the understanding of tornado-like loading on bluff bodies, most of those studies focused on the mean component of the loading and the peak loading. Detailed characteristics of the fluctuating component of the loading, such as the variation of the statistical moments of the pressures on the surface of the bluff bodies, which are important for understanding the loading on components and claddings of structures, and the corresponding statistical moments of the resultant forces were not provided. In addition, the characteristics of the loading fluctuation were often not interpreted in the context of the fluctuating component of the tornado-like winds and the corresponding fluctuation of the static pressure. To further the understanding of tornado-like loading on bluff bodies, two rectangular prisms of various configurations were tested at multiple radial locations in a two-celled tornado-like vortex generated by a large-scale Ward-type simulator. This paper presents an interpretation of the measured pressures and forces acting on the prisms in the context of the velocity and static pressure fields of the simulated tornado-like vortex. The effects of the radial location and elevation of the prisms, as well those of the depth to height ratio of the prisms on the tornado-like loading are examined. The outcomes of this study can help advance the understanding of the interaction between tornadic winds and bluff bodies. In addition, along with previous studies of tornado-like loading on bluff bodies of generic shapes (e.g., Rajasekharan et al., 2013) the statistics of the pressures and resultant forces acting on the prisms, as well as the dependence of these statistics on the influencing factors can be used as benchmarks that results from other laboratory and numerical studies can be compared with.

2. Experimental configurations

2.1. Experimental facility and simulated tornado-like flow

The experiments were conducted in a Ward-type tornado simulator, known as VorTECH, at Texas Tech University. As schematically shown in Fig. 1, the simulator has an updraft hole of 4 m in diameter and a testing chamber of 10.2 m in diameter. The height of the testing chamber as well as those of the turning vanes installed around the periphery of the

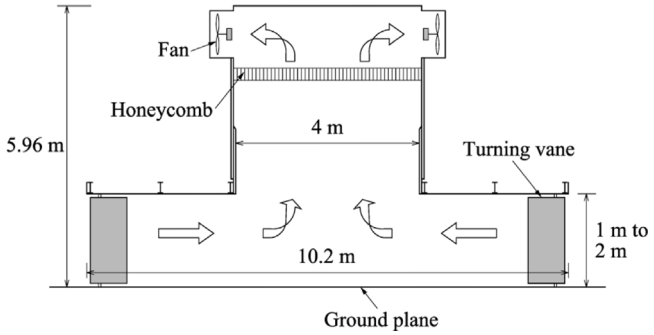

Fig. 1. A schematic illustration of VorTECH (Tang et al., 2018a).

chamber to control the circulation of the inflow can be varied between 1 m and 2 m, depending on the desired aspect ratio of the simulation. The updraft is provided by 8 fans at the top of the simulator. More details regarding the specifications and features of VorTECH as well as evidence of its capability in simulating tornado-like vortices of various types can be found in Tang et al. (2018a,b).

The tornado-like vortex in which the prims were tested was simulated at a swirl ratio of $S = 0.83$, an aspect ratio of $a = 0.5$ and a radial Reynolds number of $Re_r = 5.51 \times 10^5$. The definitions of the swirl ratio, aspect ratio and Reynolds number used in this study follow those given in Church et al. (1979), that is,

$$S = r_0 \Gamma/(2Qh) \tag{1}$$

$$a = h/r_0 \tag{2}$$

$$Re_r = Q/(2\pi\nu) \tag{3}$$

where Q is the volume flow rate per unit axial length, Γ is the circulation, h and r_0 are the height of the turning vanes and the radius of the updraft hole, respectively, and ν is the kinematic viscosity of air. It is noted herein that while the definition of the radial Reynolds number in the main text of Church et al. (1979) is in the form of equation (3), the definition of the same parameter in the appendix of the same paper does not have the factor 2π in the denominator. For the calculation of the swirl ratio and the radial Reynolds number, the volume flow rate per unit axial length and the circulation are estimated in this study based on measurements of flow velocity at points along a vertical line originating from the edge of the updraft hole, following the scheme used by Tang et al. (2018a).

To characterize the simulated tornado-like flow, a Cobra Probe (Turbulent Flow Instrumentation) and an Omni Probe (Aero Probes) were used to measure the velocities at predetermined locations over an area of a vertical plane through the vertical axis of the simulator at a sampling frequency of 625 Hz. The Cobra probe was used when at least 98% of the data were considered valid by the software provided by the manufacturer; otherwise, the Omni Probe was used. In addition, a ZOC33 scanner of a Scanivalve system was used to measure the pressures at 289 taps along a radial line on the floor of the simulator (within ± 1.9 m from the center) at a sampling frequency of 625 Hz. The velocity measurement at each location was conducted once for a duration of 2 min. The surface pressure measurement was repeated 10 times, each time for a 2-minute duration, to provide an ensemble of measurements for the estimation of statistics. Fig. 2(a) shows the mean velocity field of the simulated vortex over the area of measurement, and Fig. 2(b), (c) and (d) show the turbulence intensity, skewness and kurtosis of the tangential velocity over the region in which the Cobra probe was used for the measurement. In these graphs, the normalized radial position $\lambda_p = r/r_c$, where r is the radial distance from the vertical axis of the simulator and $r_c = 46$ cm is the radial distance at which the mean tangential velocity of the flow reaches the maximum magnitude (subsequently referred to as the core radius), z is the height above the floor, and $z_c = 6$ cm is the height at which the mean tangential velocity of the flow reaches the maximum magnitude, $(\overline{V}_\theta)_{\max}$. For all four graphs, the color represents the quantities resulted from a linear interpolation of the statistics estimated based on the velocity measurements; the arrows in Fig. 2(a) represent the resultants of the mean radial (i.e., toward the center of the simulator) and axial (i.e., in the vertical direction) components of the velocities at the points of measurements. The turbulence intensity of the tangential velocity shown in Fig. 2(b) are defined as $\sigma_{v_\theta}/\overline{V}_\theta$, in which σ_{v_θ} and $\overline{V}_\theta$ are the standard deviation and mean value of the tangential velocity.

The down draft around the axis of the vortex that reaches the simulator floor, as seen in Fig. 2(a), signifies that the simulated vortex is two-celled in structure. It is also seen in Fig. 2(a) that over the lower heights (say, when $z < 15$ cm), the size of the core of the vortex, represented by the radial position at which the maximum magnitude of the mean tangential velocity at a given height occurs, expands with increasing height. In addition, Fig. 2(b), (c) and (d) suggest that the tangential component of the flow becomes more turbulent and the turbulence of this component exhibits non-Gaussian features as the flow approaches the core of the vortex from the inlet side of the simulator.

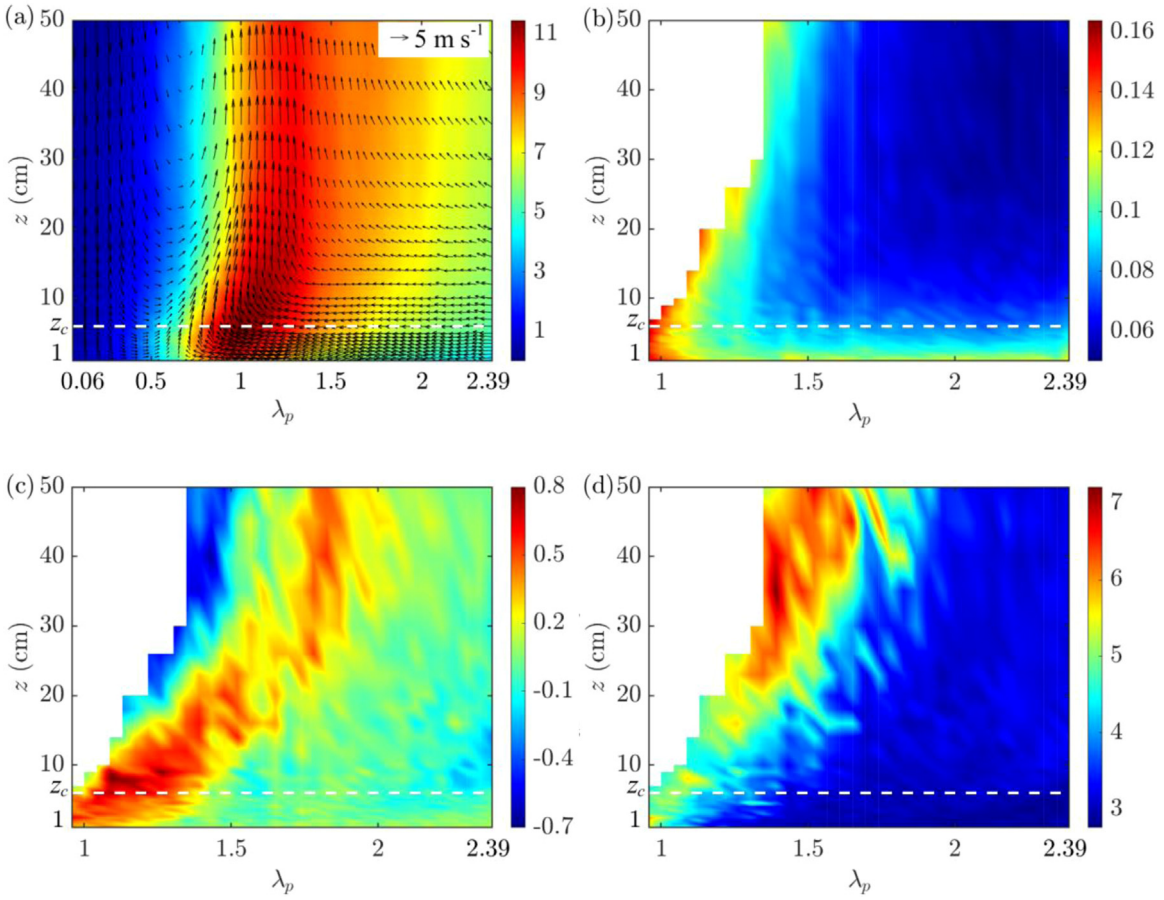

Fig. 2. (a) Mean velocity components (in m/s), and (b) the turbulence intensity, (c) skewness and (d) kurtosis of the tangential velocity of a part of the tornado-like flow.

In addition to the velocities of the flow, the Cobra Probe also provided measurements of the static pressure of the air. Fig. 3 displays the mean value, standard deviation, skewness and kurtosis of the static pressure coefficients over the region in which the Cobra Probe was used for the measurement. The static pressure coefficient is defined as

$$C_p = (P - P_{ref})/[\rho(\overline{V}_\theta)^2_{\max}/2] \tag{4}$$

where P is the static pressure, P_{ref} is the reference pressure, taken as the ambient static pressure in the work space underneath the simulator (subsequently referred to as the pit), and ρ is the air density. It is apparent that the rotation of the flow has created significant static pressure deficit over the areas of the measurement. According to Fig. 3(a), the mean static pressure deficit is large in the region surrounding the axis of the vortex. In addition, Fig. 3(b), (c) and (d) suggest that the fluctuation of the static pressure intensifies as the flow approaches the core of the vortex, and the fluctuation exhibits significant non-Gaussian characteristics in the regions surrounding the core of the vortex. These characteristics of the static pressure are similar to the corresponding characteristics of the flow velocity.

The characteristics of the near ground flow are also reflected in the pressures on the floor of the simulator. Fig. 4 shows the mean values, standard deviations, skewness values and kurtosis values of the coefficients of the pressures at the locations of the taps (normalized by the core radius) on the simulator floor, which is defined in the form of the static pressure coefficients of the air (Eq. (4)) except that P in this case is the pressure on the floor. Like the static pressure of the flow aloft, the surface pressure can be very different from the barometric pressure in the pit. In particular, an examination of Fig. 4(a) in the context of Fig. 3(a) reveals that the mean static pressure deficits of the flow over the regions of the lowest level of the Cobra Probe measurements are close to the mean surface pressure deficits at the corresponding radial locations. The two valleys in the radial profile of the mean surface pressure deficit shown in Fig. 4(a) and the bimodal shape of the standard deviation of the surface pressure fluctuation shown in Fig. 4(b) are another two pieces of evidence that the vortex is two-celled in structure (Pauley et al., 1982; Tang et al., 2018a). In addition, Fig. 4(b) reveals that the surface pressures in the areas inside and immediately surrounding the core radius exhibit intense fluctuations, and Fig. 4(c) and (d) suggest that the fluctuations of the surface pressure in these areas can be highly non-Gaussian in characteristics,

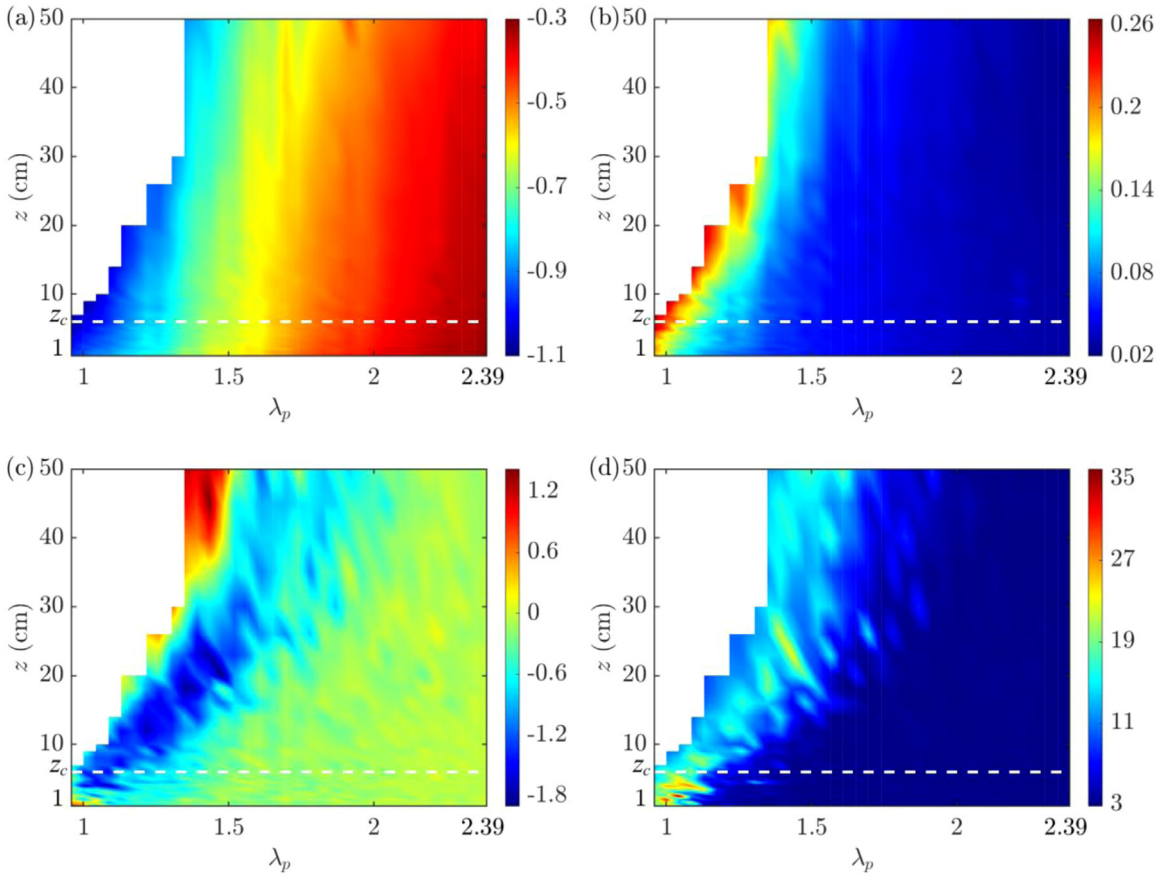

Fig. 3. (a) Mean values, (b) standard deviations, (c) skewness, and (d) kurtosis of the static pressure of a part of the tornado-like flow.

although the fluctuations of the surface pressures in the areas far outside the core radius exhibit Gaussian characteristics. As will be seen subsequently, all these characteristics of the surface pressure fluctuations and those of the flow aloft are manifested in the tornado-like loading on the prisms.

2.2. Models and test configurations

Two plastic prisms built using 3D printing technology were tested in the experiments. Fig. 5 schematically shows a typical configuration of a prism with a width of b, a depth of t and a height of h that is elevated from the simulator floor with a clearance of c. Both prisms have a width of $b = 10$ cm and a height of $h = 5$ cm, which corresponds to a width to height ratio of $\lambda_b = b/h = 2$. The depths of the two prisms are $t = 5$ cm and 2.5 cm, respectively, which gives depth to height ratios ($\lambda_t = t/h$) of 1.0 and 0.5, respectively.

Each prism was tested at four radial locations of $r = 0$, $r = 0.5r_c$ $r = r_c$, and $r = 2r_c$, respectively, which correspond to normalized radial positions ($\lambda_p = r/r_c$) of 0, 0.5, 1.0, and 2.0, respectively. At each radial location, the prisms were aligned in the radial direction (i.e., with the longitudinal axis of the prism, in the direction of its length, being along the radial coordinate of the simulator) and tested both on the floor (i.e., unelevated) and with clearances of 0.25 cm, 0.5 cm, 1 cm and 2.5 cm, respectively, above the simulator floor, which correspond to clearance ratios ($\lambda_c = c/h$) of 0, 0.05, 0.1, 0.2, and 0.5, respectively. Testing of the prisms at the different clearance ratios, in particular, allows an evaluation of the loading variation due to the variation of the flow at different elevations as well as the influence of the clearance on the loading, which has been observed to be significant in the case of loading on rectangular sign structures by boundary-layer type winds (e.g., Letchford, 2001; Smith et al., 2014; Zuo et al., 2014). When the models were situated on the simulator floor, the edges of the bottom face were sealed so that the interface between this face and the floor was airtight. The elevated models were supported at the center of the bottom faces by aluminum rods of 1 cm in diameter. The prisms were also tested with the same location and elevation configurations described above but with their longitudinal axes being perpendicular to the radial coordinate of the simulator. The tornado-like loading was expectedly found to depend on the prism orientation. However, this paper only focuses on the case when the longitudinal axes of the prisms are along a radial line of the simulator. It must also be noted that the experiments were conducted on a nominally smooth

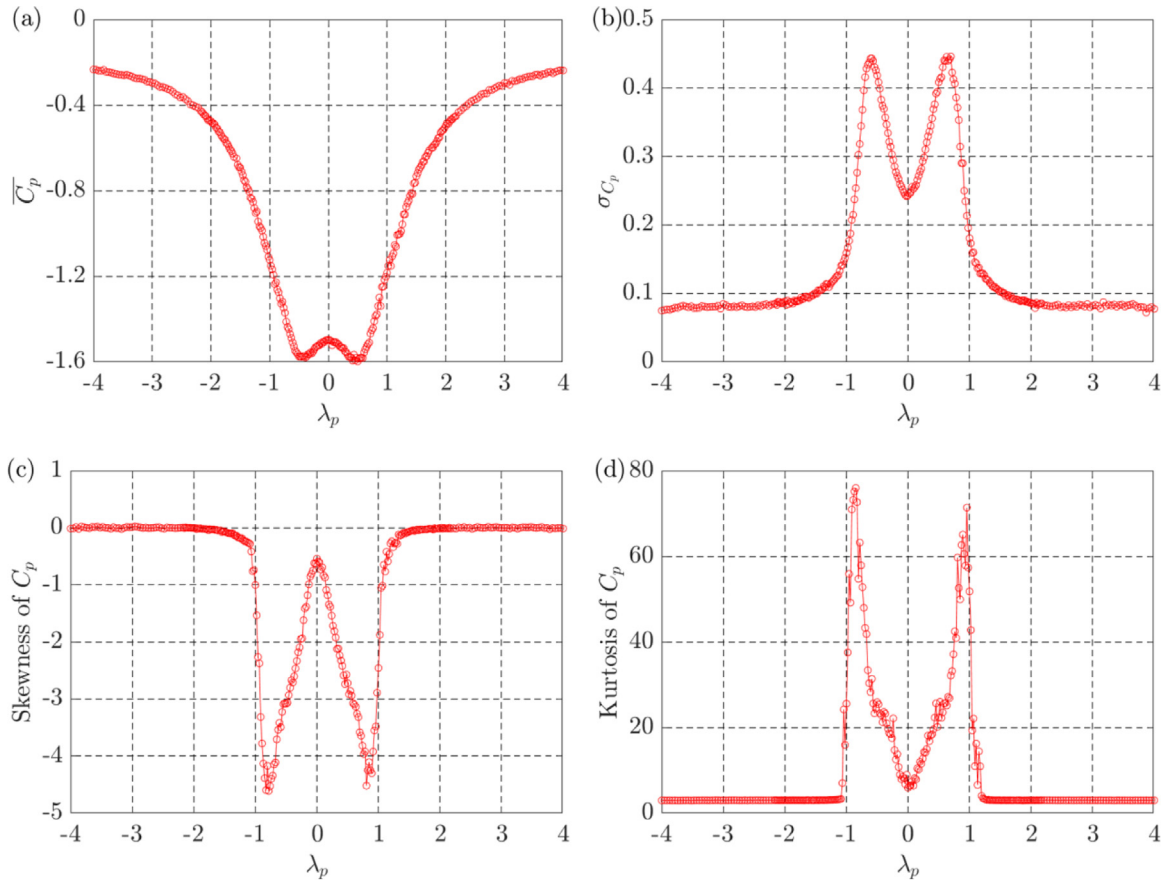

Fig. 4. (a) Mean values, (b) standard deviations, (c) skewness, and (d) kurtosis of the pressure deficits along a radial line on the floor of the simulator.

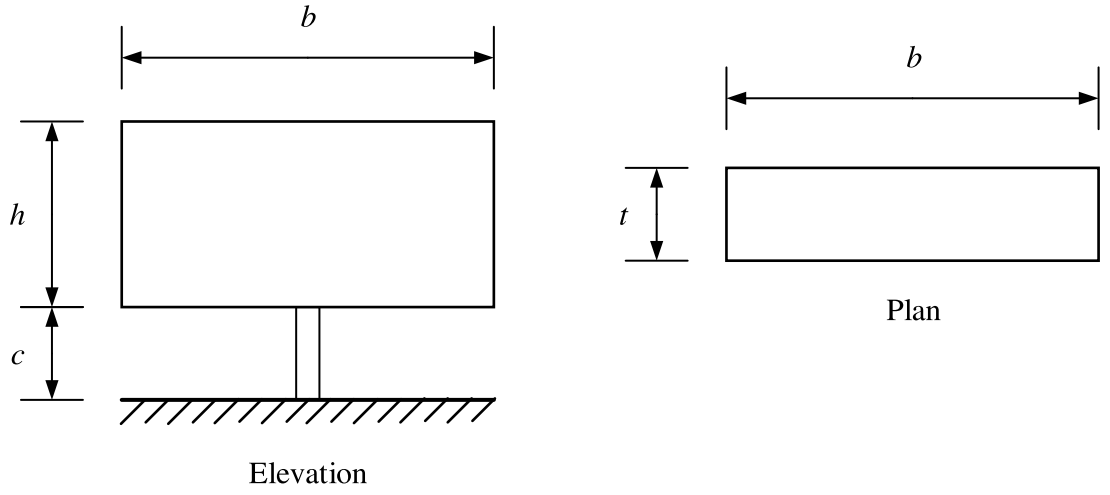

Fig. 5. Schematics of prisms tested in the experiments.

surface beneath a tornado-like vortex that does not translate relative to the rectangular prisms. Therefore, the loading on the prisms does not account for the effects of the roughness of the surrounding surface or those of tornado translation, which can be significant according to precious studies of tornado-like loading on bluff bodies such as models of low-rise buildings (e.g., Haan et al., 2010; Sabareesh et al., 2012).

Table 1
Specifications of the force/torque transducer.

Ranges			Resolutions		
F_x, F_y	F_z	T_x, T_y, T_z	F_x, F_y	F_z	T_x, T_y, T_z
32 N	100 N	2.5 N m	1/160 N	1/80 N	1/2000 N m

F_x and F_y: forces along the horizontal axes; F_z: force along the vertical axis;
T_x and T_y: torque about the horizontal axes; T_z: torques about the vertical axis.

The tornado-like loading on the elevated prisms was measured by a six-component (i.e., forces along two orthogonal horizontal axes and a vertical axis and torques about these three axes) ATI-IA force/torque transducer (Gamma series, with a "SI-32-2.5" calibration) that was connected to the aluminum rods supporting the models. The ranges and resolutions of the components of the force/torque transducer are listed in Table 1. When the prisms were unelevated, the loading was measured by pressure taps that were sampled by a Scanivalve ZOC33 pressure scanner. Fig. 6 shows the layouts of the pressure taps on the two models.

For illustration, Fig. 7 shows the prism with a depth to height ratio of 0.5 mounted at an elevated position and the prism with a depth to height ratio of 1.0 mounted on the simulator floor. For each test configuration of each prism, the force or pressure measurement was repeated 10 times, and the duration of each measurement was 2 min. The sampling frequency for both type of measurement is 625 Hz. Since the statistics of the measurements do not vary significantly among the individual test runs, only the mean values of the statistics estimated based each of the 10 repeat test runs are presented in the following.

3. Results

A local coordinate system with its origin at the intersection of the vertical axis of the prism of interest and the simulator floor (Fig. 8) is used in the following to facilitate an interpretation of the loading on the prisms. The tornadic forces acting on the prisms are represented by the three components, F_r, F_θ and F_z, along the axes in the radial (r), tangential (θ) and vertical (z) directions, respectively. When the prisms were tested on the simulator floor, the pressures at the locations of the pressure taps are represented by pressure coefficients as defined in the form of Eq. (4), except that $P_i(t)$ in this case is the total pressure at the pressure tap of interest at time t. The pressure measurements are also used as a basis to compute the force components according to the following equations:

$$F_r(t) = -\sum_{j=1}^{n_r} \mathrm{sgn}(r_j) P_j(t) A_j; \quad F_\theta(t) = -\sum_{k=1}^{n_\theta} \mathrm{sgn}(\theta_k) P_k(t) A_k; \quad F_z(t) = -\sum_{l=1}^{n_z} \mathrm{sgn}(z_l) P_l(t) A_l \tag{5}$$

in which n_r, n_θ and n_z are the numbers of pressure taps on the faces that are perpendicular to the axes in the radial, tangential and vertical directions, respectively. $P_j(t)$, $P_k(t)$ and $P_l(t)$ are the pressures at tap j with coordinates (r_j, θ_j, z_j) on the faces that are perpendicular to the radial axis, tap k with coordinates (r_k, θ_k, z_k) on the faces that are perpendicular to the tangential axis and tap l with coordinates (r_l, θ_l, z_l) on the faces that are perpendicular to the vertical axis, respectively, and A_j, A_k and A_l are the tributary areas of taps j, k and l, respectively. The function "sgn()" in Eq. (5) gives a value of positive one if its argument is positive and negative one if its argument is negative.

The force components computed based on the pressure measurements, as well as the force components measured directly by the force transducer are represented by corresponding coefficients defined as

$$C_{F_r} = F_r/(\rho \overline{V}^2_{\theta\,\max} A_r/2); \quad C_{F_\theta} = F_\theta/(\rho \overline{V}^2_{\theta\,\max} A_\theta/2); \quad C_{F_z} = F_z/(\rho \overline{V}^2_{\theta\,\max} A_z/2) \tag{6}$$

where $\overline{V}_{\theta\,\max}$ is the largest mean tangential velocity in the flow field of the vortex without the presence of the prisms, A_θ, A_r and A_z are the areas of the faces of the prism of interest that are perpendicular to the tangential, radial and vertical directions, respectively, and C_{F_r}, C_{F_θ} and C_{F_z} are the coefficients of the force components in the radial (r), tangential (θ) and vertical (z) directions, respectively. In the following, the effects of the radial locations at which the prisms are tested as well as those of the depth-to-height and clearance ratios of the prisms on the tornado-like loading are presented.

3.1. Effects of the radial location of the prisms on the tornado-like loading

Due to the significant spatial variation of the mean and fluctuating components of the wind speed and static pressure in the simulated vortex, both the mean and the fluctuating components of the tornado-like loading on the prisms are highly dependent on the radial location. However, some of the dependencies are similar regardless of the depth to height ratio and clearance ratio of the prism. In the following, the characteristics of the mean and fluctuating components of the tornado-like loading in terms of the pressures and the resultant forces on the two unelevated prisms (i.e., $\lambda_c = 0$) are presented to illustrate the effects of the radial location of the prisms on the tornado-like loading.

Fig. 9 shows the mean coefficients of the pressures acting on the faces of the prism with a unit depth to height ratio (i.e., $\lambda_t = 1.0$) when it is unelevated. It is apparent that for all the four radial locations at which the prism was tested,

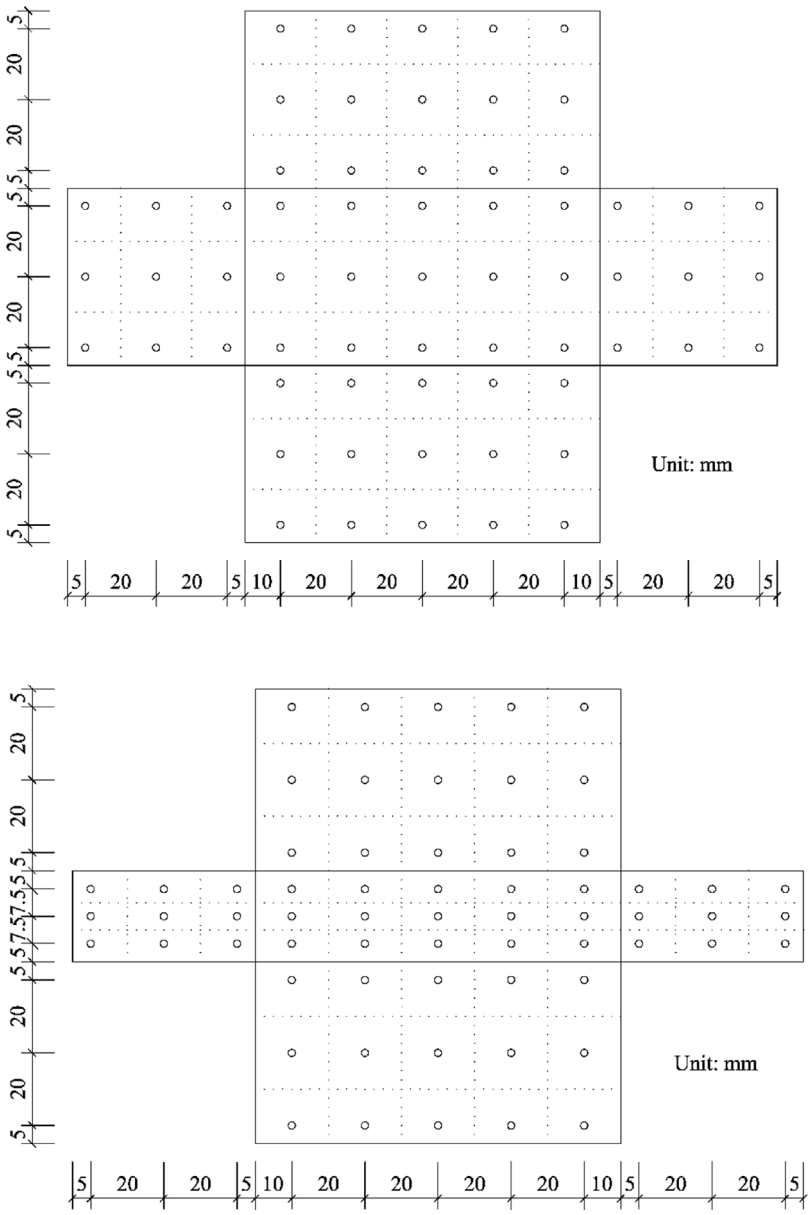

Fig. 6. Layouts of the pressure taps on the prisms.

the mean pressure at every tap is negative. This prominent characteristic of the loading is a result of two facts: (1) that the swirling of the flow creates significant mean static pressure deficits, as indicated by Fig. 4, and (2) that for the same reference pressure, the magnitudes of the mean static pressures are larger than the magnitudes of the corresponding mean aerodynamically induced pressures. It must be noted that the presence of the prism inherently alters the tornado-like flow field (e.g., Kopp and Wu, 2020). Nevertheless, Fig. 9 indicates that the altered flow field still creates large static pressure deficit as compared to the barometric pressure in the pit beneath the simulator.

Fig. 9 also clearly shows the significant differences among the mean characteristics of the tornado-like loading at the four radial locations. When the prism is at the center of the simulator floor (i.e., $\lambda_p = 0$), the distribution of the mean pressures acting on a side face is approximately (not exactly, due to the imperfection of the experiment) antisymmetric to the distribution of the mean pressures acting on the opposite face, and the mean pressures acting on the top face are approximately antisymmetric about the two horizontal axes of this face. These are reflections of the fact that the simulated vortex is nominally axisymmetric but the mean flow rotates in the counterclockwise direction. Furthermore, it can be seen that when the prism is at the center of the simulator floor, the mean pressures acting on its faces vary only over a narrow range that are quite close to the range of rather uniform mean pressures on the part of the simulator floor

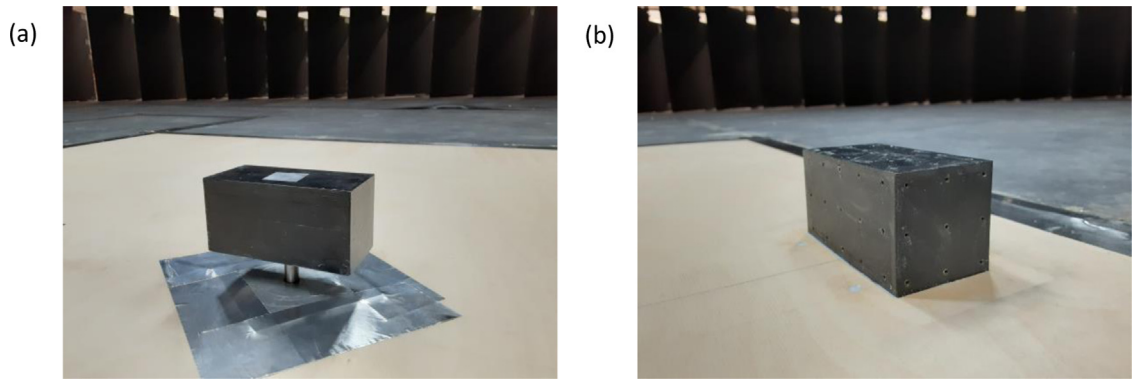

Fig. 7. (a) The prism with a depth to height ratio of 0.5 at an elevated position and (b) the prism with a depth to height ratio of 1.0 situated on the simulator floor.

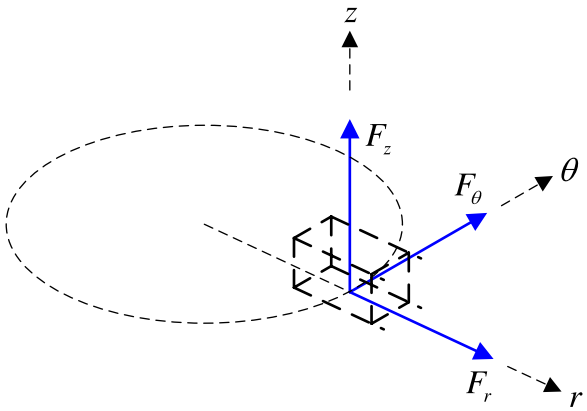

Fig. 8. Schematic of the components of the force acting on a prism.

when the prism is not present (Fig. 4(a)). This is because the mean velocities of all three components of the near-floor (e.g., less than 10 cm above the simulator floor) flow in the region surrounding the axis of the vortex (Fig. 2) are all low. Because the velocities of the flow in this region are low, the mean structure of the flow surrounding the small prism is not likely to be significantly different from the mean structure of the flow in the same region when the prism is not present. Consequently, the mean pressures acting on the prism at this location are expected to be similar to the pressures of the air in this region.

By contrast, Fig. 9 shows that when the prism is at the three radial locations away from the axis of the vortex (i.e., $\lambda_p = 0.5$, $\lambda_p = 1.0$, and $\lambda_p = 2.0$, respectively), the mean pressures acting on its faces vary over broad ranges and can be very different from the mean static pressures over those regions without the presence of the prism (Figs. 3(a) and 4(a)). This is because the velocities of the near-floor flow over those regions can reach much higher magnitudes than can the velocities of the near-floor flow surrounding the axis of the vortex and, for this reason, the aerodynamically induced pressures of the flow surrounding the prism at the three radial locations away from the axis of the vortex can contribute significantly to the total pressures acting on the prism. In particular, it can be observed in Fig. 9 that when the prism is at the three locations away from the axis of the vortex, the magnitudes of the negative mean pressures acting on face 2, which is on the windward side relative to the mean direction of the tangential velocity, is much smaller than the magnitudes of the negative mean pressures acting at the mirroring locations on face 4, which is on the leeward side relative to the mean direction of the tangential velocity. This is a result of the positive mean aerodynamically induced pressures acting on the windward face partially offsetting the negative mean static pressures and the negative mean aerodynamically induced pressures deficits on the leeward face adding to the negative mean static pressure deficits. In this sense, it is not surprising to see that the largest differences of the magnitudes of the mean negatives pressures on faces 2 and 4 occurs when the prism is one core radius away from the axis of the vortex because the mean tangential velocities are the largest over this region. Similarly, it can be observed in Fig. 9 that when the prism is one core radius and two core radii away from the axis of the vortex (i.e., $\lambda_p = 1.0$, and $\lambda_p = 2.0$, respectively), the magnitudes of the negative mean pressures acting on face 3 are markedly smaller than the magnitudes of the pressures at the mirroring locations on face 1 primarily because faces 3 and 1 are on the windward and leeward sides relative to the mean direction of the radial velocity at these locations.

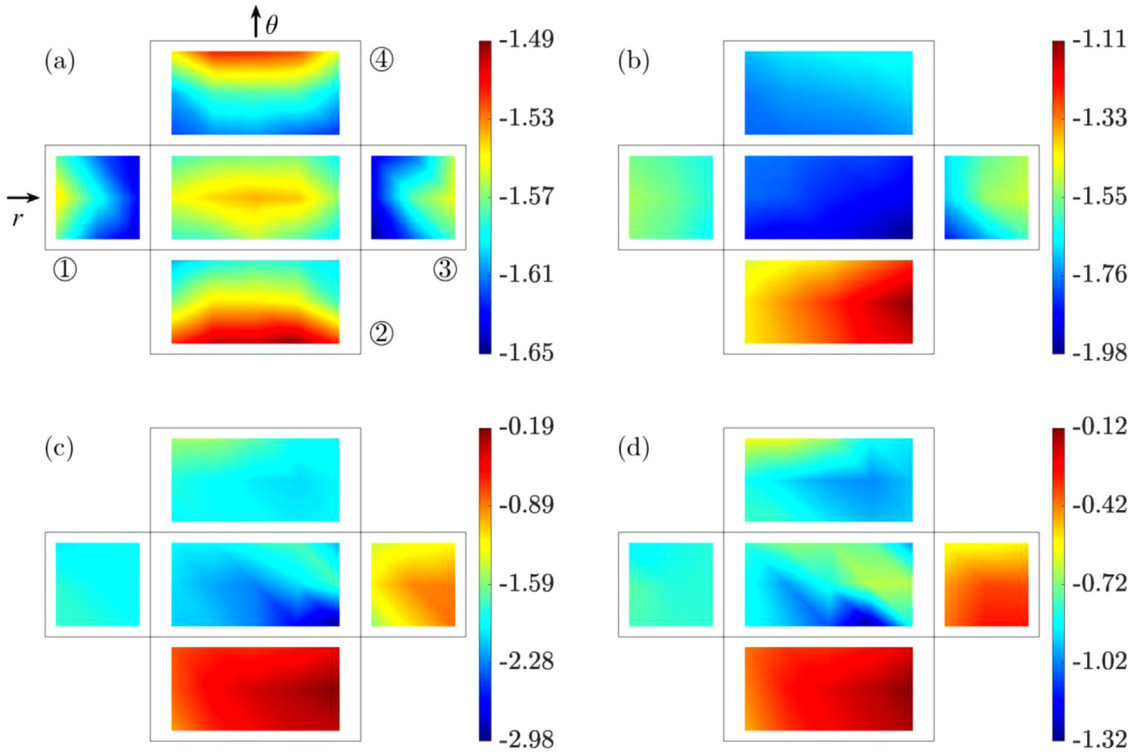

Fig. 9. Mean coefficients of the pressures acting on the faces of the prism with a unit depth to height ratio when it is situated at four radial locations on the simulator floor: (a) $\lambda_p = 0$, (b) $\lambda_p = 0.5$, (c) $\lambda_p = 1.0$, and (d) $\lambda_p = 2.0$.

Moreover, Fig. 9 suggests that at each of the three radial locations away from the axis of the vortex, the mean negative pressures of the largest magnitudes occur on the top face of the prism. This is primarily due to the aerodynamically induced pressure caused by the separation of the flow from the faces on the windward side relative to the mean direction of the horizontal flow component (e.g., faces 2 and 3 when the prism is one core radius away from the axis of the vortex). In particular, it is seen that the mean negative pressure of the largest magnitude, which is much larger than the static pressure deficit in this region without the presence of the prism (Fig. 3(a)), occurs on the top face of the prism when the prism is one core radius away from the axis of the vortex because the mean tangential velocities of the flow are the highest over this region (Fig. 2). By contrast, when the prism is two core radii from the axis of the vortex, the magnitudes of the mean negative pressures on its top face are much smaller because both the horizontal velocities and the static pressure deficit over this region are of small magnitudes.

Fig. 10 shows the standard deviations of the coefficients of the pressures acting on the prism when it is at the four locations on the simulator floor. It is evident that the fluctuations of the pressures can be much more intense when the prism is at locations that are one or one half of the core radius from the axis of the vortex (i.e., $\lambda_p = 1.0$ or $\lambda_p = 0.5$) than when it is at the other two locations. This can be attributed to not only the high intensity fluctuations of the static pressure and wind velocity over these regions (Figs. 2(b), 3(b) and 4(b)), but also the fact that the signature turbulence caused by the separation of the high-velocity flow from the prism at these two locations also contributes to the fluctuation of the loading. The facts that the loading on the prism is primarily due to the static pressure when the prism is at the axis of the vortex and that the aerodynamically induced pressure contributes significantly to the total loading when the prism is at the other three radial locations are also reflected Fig. 10. When the prism is at the axis of the vortex (i.e., $\lambda_p = 0$), the standard deviations of the coefficients of the pressures acting on its faces are over a narrow range that is similar to the range of the coefficients of the pressures acting on this portion of the floor without the presence of the prism (Fig. 4(b)). By contrast, when the prism is at any of the three radial locations away from the axis of the vortex (i.e., $\lambda_p = 0.5$, $\lambda_p = 1.0$, and $\lambda_p = 2.0$) the fluctuations of the pressures acting on the prism are over much broader ranges, and the pressure fluctuations of the highest intensities occur over the areas immediately following the edge from which the flow is expected to separate from the prism. For example, when the prism is at the core radius location, the pressure fluctuations of the highest intensities are over an area on the top face that is close to the vortex where the top face meets faces 2 and 3. This is not surprising because the flow field at this location has high values for both the tangential and radial velocity components (Fig. 2).

Figs. 11 and 12 show the values of the skewness and kurtosis, respectively, of the pressures acting on the faces of the prism for the four locations on the simulator floor at which it was tested. It can be seen that when the prism is at

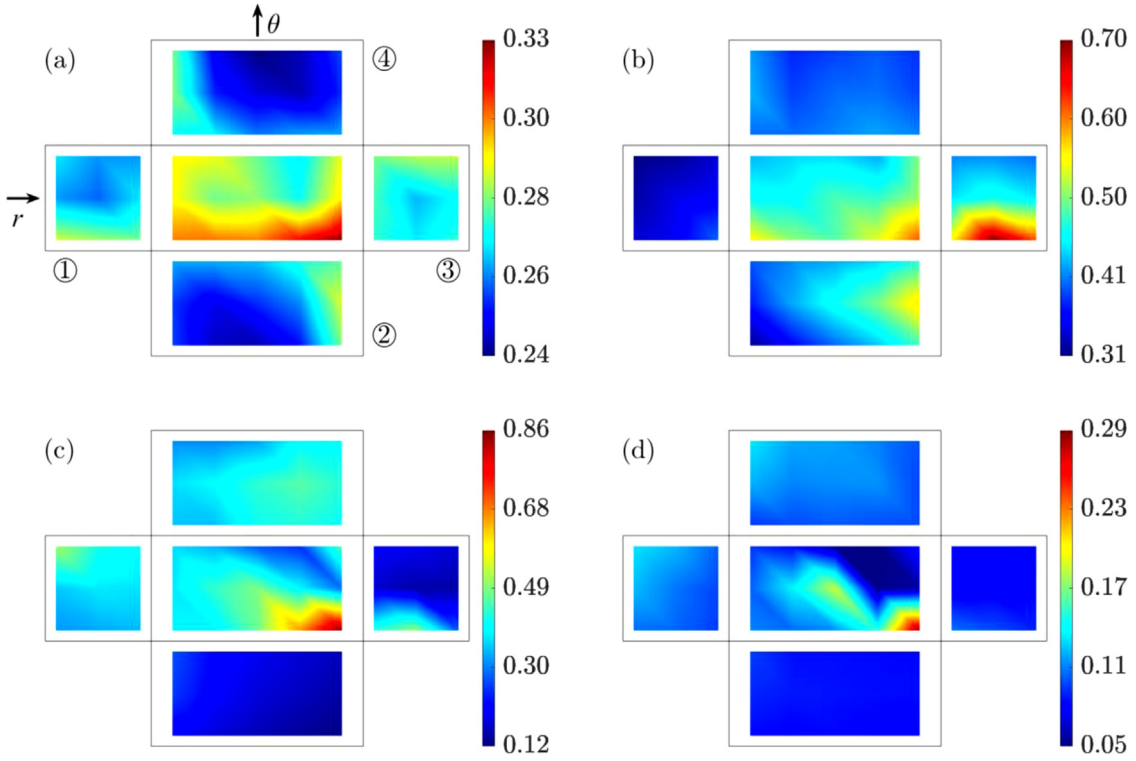

Fig. 10. Standard deviations of the pressures acting on the faces of the prism with a unit depth to height ratio when it is situated at four radial locations on the simulator floor: (a) $\lambda_p = 0$, (b) $\lambda_p = 0.5$, (c) $\lambda_p = 1.0$, and (d) $\lambda_p = 2.0$.

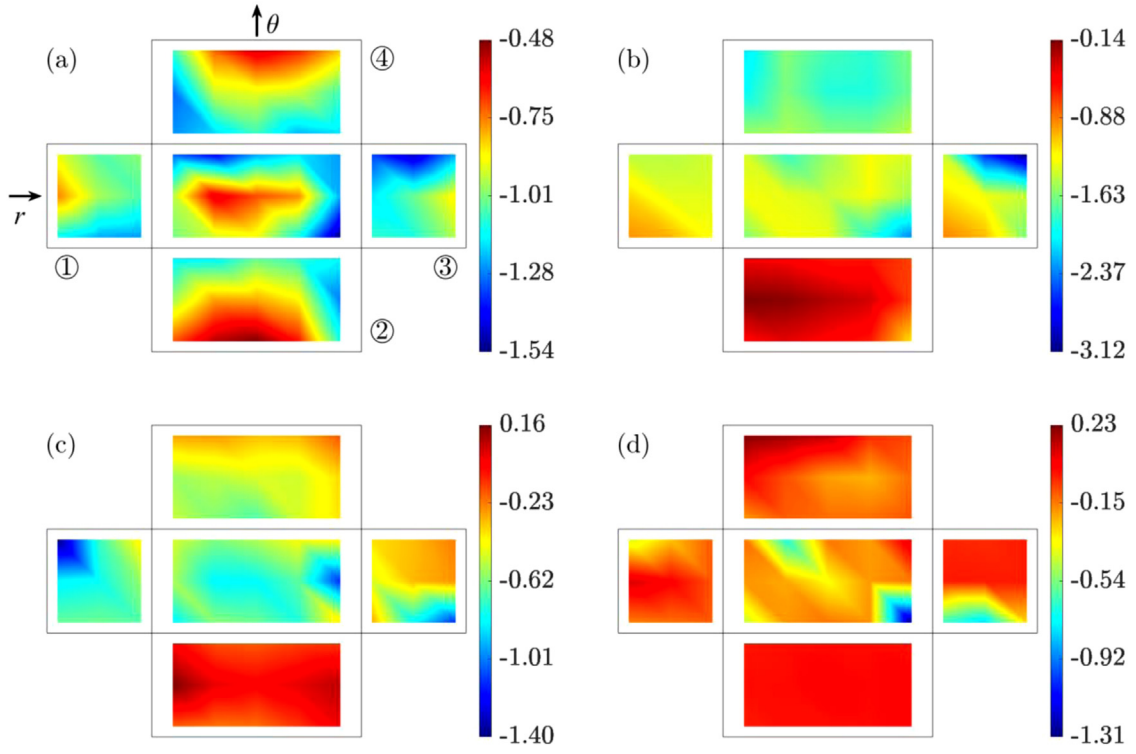

Fig. 11. Skewness of the pressures acting on the faces of the prism with a unit depth to height ratio when it is situated at four radial locations on the simulator floor: (a) $\lambda_p = 0$, (b) $\lambda_p = 0.5$, (c) $\lambda_p = 1.0$, and (d) $\lambda_p = 2.0$.

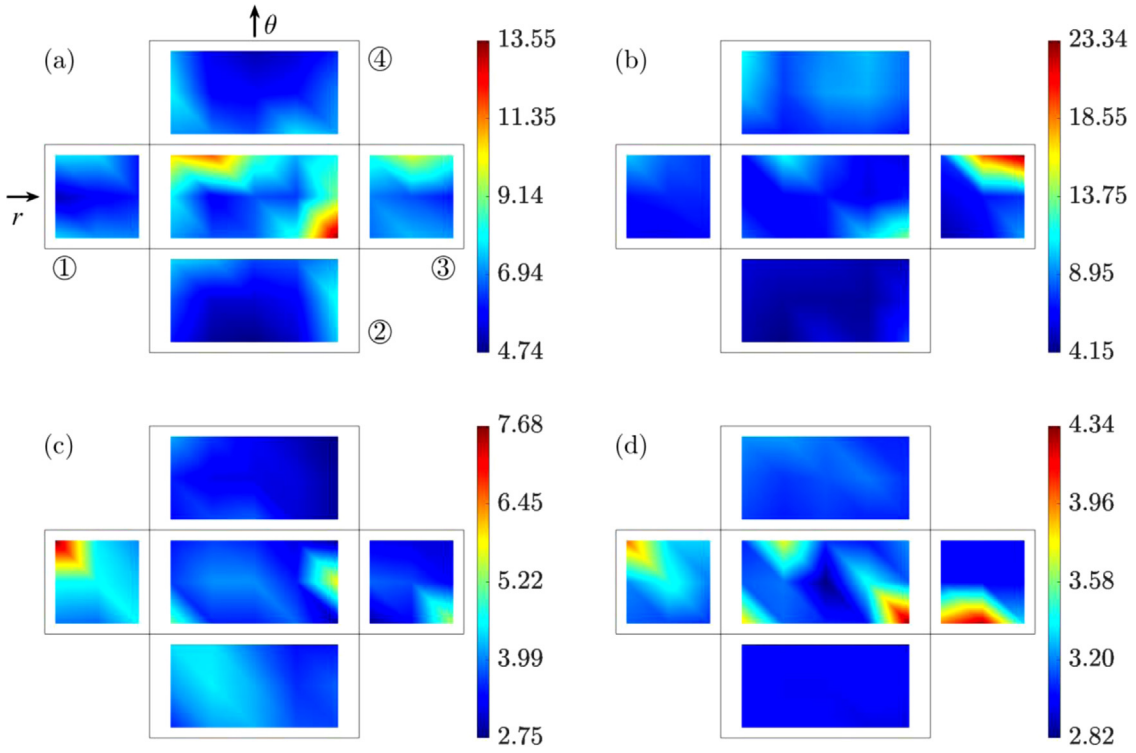

Fig. 12. Kurtosis of the pressures acting on the faces of the prism with a unit depth to height ratio when it is situated at four radial locations on the simulator floor: (a) $\lambda_p = 0$, (b) $\lambda_p = 0.5$, (c) $\lambda_p = 1.0$, and (d) $\lambda_p = 2.0$.

the three radial locations at or inside the core radius (i.e., $\lambda_p = 1.0$, $\lambda_p = 0.5$, and $\lambda_p = 0$), the skewness and kurtosis of the pressures acting on significant portions of the faces deviate significantly from zero and 3, respectively, indicating that the loading on these areas are significantly non-Gaussian in distribution. The pressures that do exhibit Gaussian characteristics when the prism is at the core radius location occur on face 2, as Figs. 11(c) and 12(c) suggest that at this location the skewness and kurtosis of the pressures over portions of face 2 are close to be zero and 3, respectively. It is particularly noteworthy that the significantly non-Gaussian loading is not restricted to the areas where the flow is separated from the prism as is the case when bluff-bodies, such as low-rise buildings, are subjected to boundary-layer type flows (e.g., Gurley and Kareem, 1997). This is because the fluctuations of both the static pressure and the velocity of the flow surrounding the prisms at these locations can be highly non-Gaussian as indicated in Figs. 2–4. By contrast, Figs. 11 and 12 also suggest that when the prism is two core radii from the axis of the vortex, the skewness and kurtosis of the fluctuation of the pressures acting on the faces of the prism are close to zero and 3, respectively, except in the areas over which the flow is separated from the prism. This is a manifestation of the fact that the fluctuations of both the static pressure and the velocity of the flow in that region, which is close to that of the boundary layer type, exhibit Gaussian characteristics (Figs. 2 and 3).

While the mean and fluctuating characteristics of the pressures acting on the unelevated (i.e., with a clearance ratio of $\lambda_c = 0$) prism with a depth to height ratio of $\lambda_t = 0.5$ will not be presented herein, the data suggest that those are qualitatively similar to the corresponding characteristics of the pressures acting on the unelevated prism with a depth to height ratio of $\lambda_t = 1$. The characteristics of the loading on the two prisms, including the differences due to the effects of the depth to height ratio, are reflected in those of the resultant forces. Fig. 13 shows the mean force coefficients of the prisms when they are unelevated. It is seen that when the prisms are at the axis of the vortex (i.e. $\lambda_p = 0$), the mean values of the force components in the tangential and radial directions are close to zero. This is expected because the mean pressures acting on the opposing side faces of the prisms at this location are approximately antisymmetric about the vertical axis, as shown in Fig. 9 for the prism with a unit depth to height ratio. Fig. 13 also shows that for the same force component acting on the same prism, the magnitude of the mean force coefficient is the largest when the prism is one core radius from the axis of the vortex. This is also expected considering, for example, the large differences between the magnitudes of the mean negative pressures acting on the opposing side faces and the mean negative pressures of large magnitudes acting on the top face when the prism with a unit depth to height ratio is at this location (Fig. 9).

In addition, Fig. 13 suggests that when the prisms are unelevated, the effect of the different depths of these two otherwise identical prisms on the mean force components is the most significant at the core radius location. This is

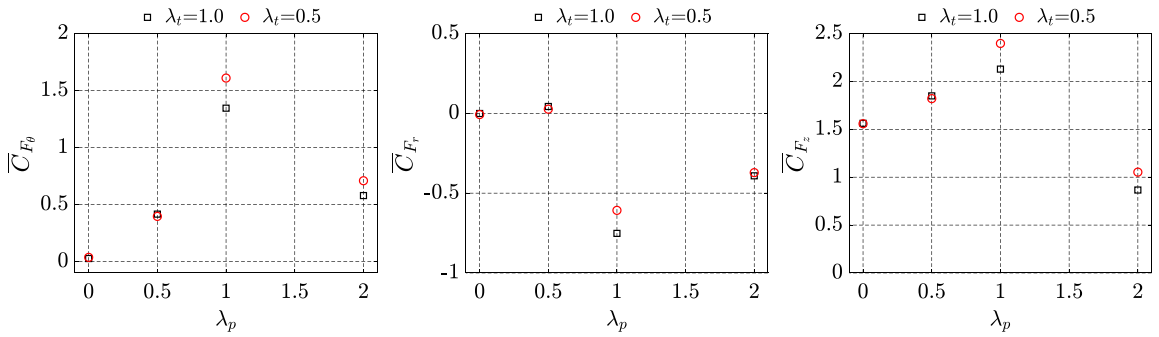

Fig. 13. Mean values of the force coefficients of the unelevated prisms.

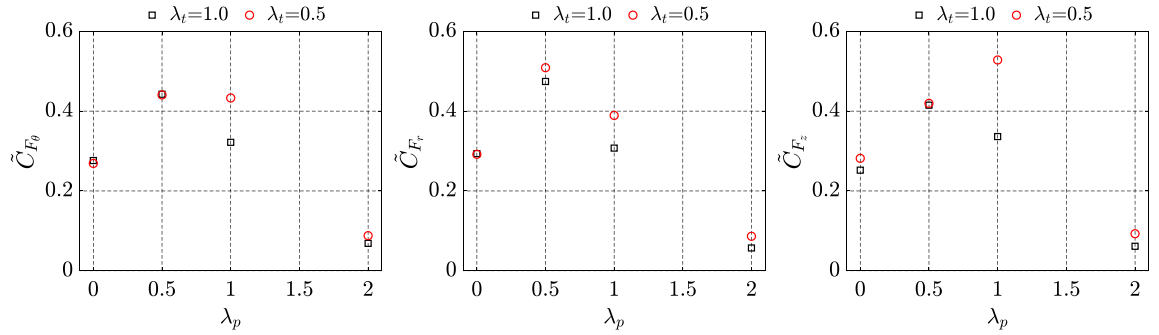

Fig. 14. Standard deviations of the force coefficients of the unelevated prisms.

because the depth to height ratio affects the aerodynamically-induced pressure by influencing the separation of the flow from the prisms (e.g., Zuo et al., 2014) and the contribution by the aerodynamically-induced pressure to the total loading is the most significant when the prisms are at this radial location (due to the high horizontal speed of the flow in this region) than at the other three radial locations.

Fig. 14 presents the standard deviations of the force coefficients of the two unelevated prisms for the four radial locations. It is seen that the fluctuation of the loading is the most intense when the prisms are one or one half of a core radius from the axis of the vortex. This is consistent with one of the observations in Fig. 10 that the fluctuations of the pressures acting on the prism with a depth to height ratio of $\lambda_t = 1.0$ are the most intense when it is at these two locations. In addition, Fig. 14 reveals that at the core radius location, the standard deviations of all three force components acting on the prism with the smaller depth to height ratio are considerably larger than the standard deviations of the force components acing on the prism with the larger depth to height ratio. This is also a consequence of the facts that the aerodynamically induced pressures contribute significantly to the total loading on the two prisms at this location and that the depth to height ratio significantly affects the aerodynamically-induced pressures by influencing the separation of the flow from the prisms.

Figs. 15 and 16 show the skewness and kurtosis of the force coefficients of the two unelevated prisms. It is seen that at the three locations that are one core radius or less from the axis of the vortex, the skewness and kurtosis of the force coefficients can deviate substantially from zero and 3, respectively, indicating that the forces acting on the prisms at these three locations can be substantially non-Gaussian. This is consistent with the indications from Figs. 11 and 12 that the pressures acting on the faces of the prisms at these three locations exhibit significantly non-Gaussian characteristics due to the facts that both the static pressures and the velocities of the flow in the regions surrounding those three locations can be highly non-Gaussian (Figs. 2–4). However, a comparison of Figs. 11 and 12 with Figs. 15 and 16 reveals that although the skewness and kurtosis of the pressures acting on the prisms at these three locations can deviate remarkably from the values for the Gaussian distribution, the skewness and kurtosis of the force coefficients are much closer to the Gaussian values. This is because the pressures acting at well-separated locations on the faces of the prisms are not well correlated. As an example, Fig. 17 shows the correlation coefficients of the pressure at a corner tap on the top face of the prism with a unit depth to height ratio then the prism is at the positions of $\lambda_p = 0$ and $\lambda_p = 0.5$ on the floor. It is seen that at both locations, the correlation coefficient becomes small when the distance between the taps becomes large.

Figs. 15 and 16 also suggest that when the prisms are two core radii from the axis of the vortex, the skewness and kurtosis values of the force components in all three directions do not deviate significantly from zero and 3, respectively, indicating that the distribution of the forces are close to Gaussian in characteristics. This is also consistent with the result

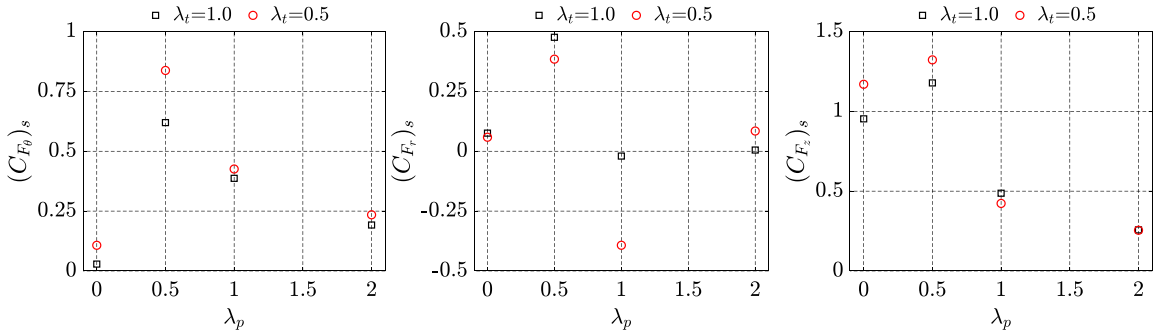

Fig. 15. Skewness of the force coefficients of the unelevated prisms.

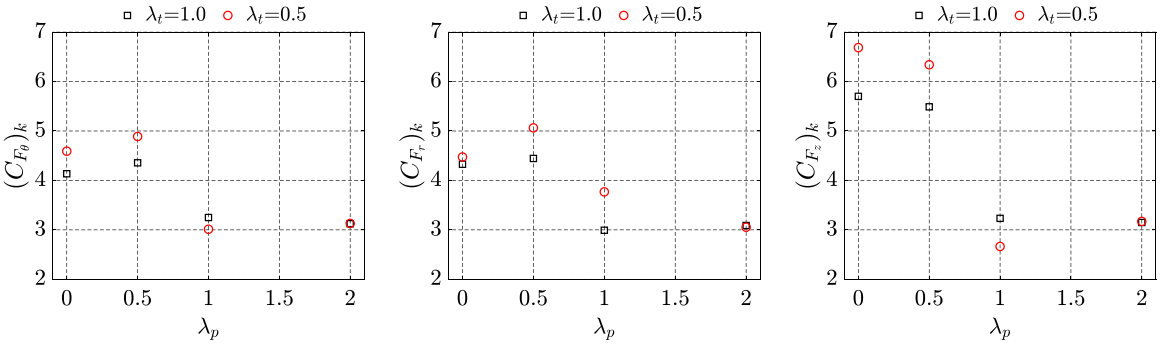

Fig. 16. Kurtosis of the force coefficients of the unelevated prisms.

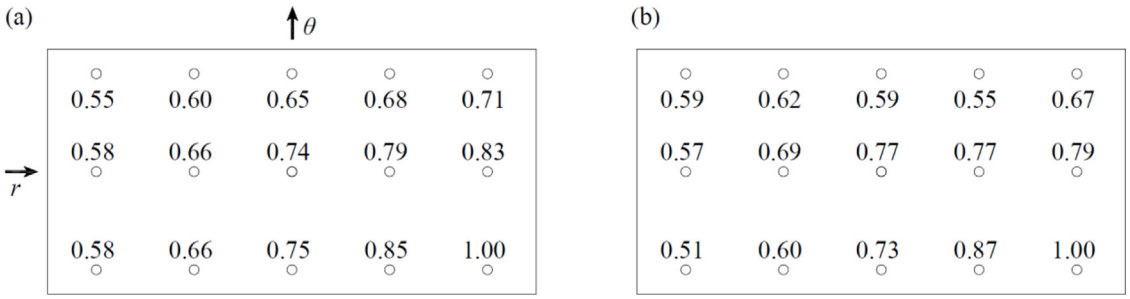

Fig. 17. Correlation coefficients of the pressures on the top face of the with a unit depth to height ratio when it is situated at four radial locations on the simulator floor: (a) $\lambda_p = 0$, (b) $\lambda_p = 0.5$.

shown in Figs. 11 and 12 for the prism with a unit depth to height ratio that except over the areas where the flow is separated from the prism the skewness and kurtosis of the pressures acting on the faces are close to the values for Gaussian distribution.

Further, Figs. 15 and 16 also indicate that except when the prisms are two core radii away from the axis of the vortex, the skewness and kurtosis of the force components acting on the two prisms of different depths can be considerably different, indicating the effects of the depth to height ratio of the prism on the characteristics of the fluctuation of the flow around the prisms. Quantification of the exact mechanism that results in these effects, however, is challenging and will not be attempted herein.

3.2. Effects of the clearance of the prisms on the tornado-like loading

In addition to the radial location, the clearance ratio also affects the tornado-like loading on the prisms. Fig. 18 shows the mean force coefficients of the prism with a unit depth to height ratio ($\lambda_t = 1.0$) at different heights above the simulator floor at the four radial locations. It is apparent that the mean vertical force is the component that is the most affected by the clearance ratio. At each radial location, the mean vertical force coefficient is much larger when the prism is unelevated (i.e., $\lambda_c = 0$) than when it is elevated (i.e., $\lambda_c > 0$). This is a clear reflection of the significant static pressure

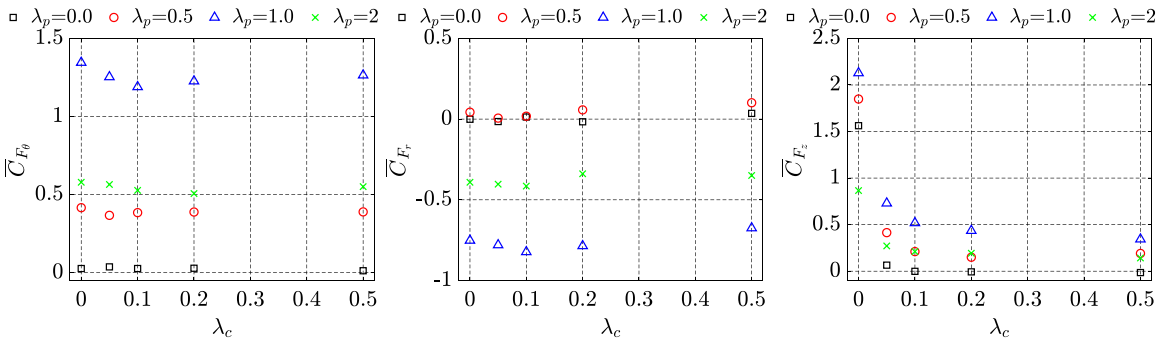

Fig. 18. Mean values of the force coefficients of the prism with a unit depth to height ratio at different radial locations and heights.

deficit in the flow and its effect on the total loading on the prism. When the prism is unelevated, the local static pressure acts on the top face but not the bottom face, resulting in a large contribution by the static pressure to the net vertical force; when the prism is elevated, even with a clearance ratio as small as 0.05, the mean static pressures acting on the bottom face mostly offset the mean static pressures acting on the top face, resulting in only an insignificant contribution to the mean net vertical force by the static pressures. Fig. 18 also suggests that for the four radial locations at which the prism is tested, the smallest difference between the mean vertical forces acting on the unelevated and elevated prism occurs when the prism is two core radii from the axis of the vortex. This is expected because the magnitudes of the mean static pressures of the flow are the smallest in the region surrounding this axial location. It must be noted, however, that the discussion above is based on the fact that the reference pressure used in the measurement of the pressures on the top face of the unelevated prism is the barometric pressure in the static bottle in the pit. If another reference pressure is used, the differences between the mean vertical forces acting on the unelevated and elevated prism will be different. Fig. 18 does also show that the mean vertical force coefficients vary with the clearance ratio when the prism is elevated. This is caused by the fact that the mean static and aerodynamically induced pressures acting on the prism changes with the height above the simulator floor, which itself is a result of the flow velocity changing with the height above the simulator floor (Fig. 2).

While the mean vertical force depends critically on whether the prism is unelevated or elevated, Fig. 18 suggests that neither this factor nor the amount of clearance under the elevated prism has a dramatic effect on the mean force components in the tangential and radial directions. In particular, it is seen when the prism is at the axis of the vortex, the mean coefficients of the tangential and radial force components essentially remain zero with varying clearance ratio. This is a reflection of the fact that the mean loading on the prism at this radial location is primarily due to the mean static pressure deficit because the mean velocity of the flow in this region is very low (Fig. 2). The relatively insignificant variations of the two horizontal force components with varying clearance when the prism is away from the axis of the vortex are primarily the results of the change in both the static pressure deficit and the velocity of the flow with changing height and the effect of the amount of clearance on the separation of the flow from the bottom face of the prism.

Fig. 19 shows the dependence of the standard deviations of the force coefficients on the clearance ratio for the prism with a unit depth to height ratio. It is seen that whether the prism is unelevated or elevated significantly affect the standard deviation of the vertical force except when the prism is two core radii away from the axis of the vortex. This is primarily due to the fact that, as indicated by Figs. 3(b) and 4(b), the fluctuation of the static pressure is likely to be much less intense in the region surrounding the radial location that is two core radii from the axis of the vortex than in the other three regions. Fig. 19 also suggests that the clearance beneath the prism can also affect the fluctuation of the two horizontal force components due to the change of the velocity and static pressure of the flow with height as well as the effect of the clearance on the flow between the bottom face of the prism and the simulator floor.

The effect of the clearance of the prism on the fluctuation of the force components is also reflected in the dependence of the skewness and kurtosis of the force components on the clearance ratio. However, an interpretation of this dependence is not attempted herein due to the challenges involved. In addition, the data from the experiments suggest that the dependences of the characteristics of the forces on the clearance ratio are qualitatively similar for the two prisms with different depth to height ratios. For this reason, the pertinent data for the prism with a depth to height ratio of 0.5 are not presented herein.

4. Conclusions

To advance the understanding of tornado-like loading on bluff bodies, two rectangular prisms of the same width and height but different depths were tested in a two-celled tornado-like vortex generated in a large Ward-type tornado simulator. In the experiments, the prisms were placed at four radial locations relative to the axis of the vortex, and the clearance of the prisms relative to the simulator floor was varied at each radial location. This enabled an assessment of the effects of the radial location and clearance of the prisms on the tornado-like loading.

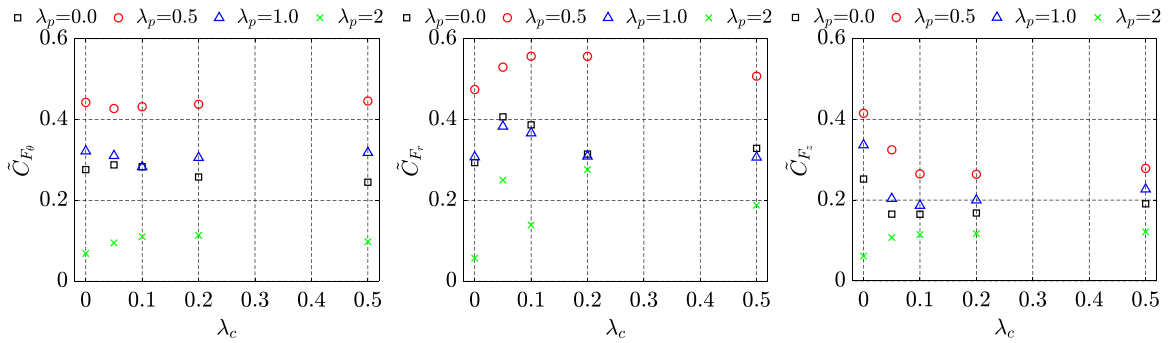

Fig. 19. Standard deviations of the force coefficients of the prism with a unit depth to height ratio at different radial locations and heights.

The data from the experiments suggest that the tornado-like loading on the prisms are highly dependent on the radial location due to the variations of the static pressure and velocity of the flow with radial location. When the prisms are at the axis of the vortex, the loading is primarily due to the static pressure deficit created by the swirling flow. As a result, the characteristics of the mean and fluctuating components of the loading are highly correlated to the corresponding characteristics of the pressure in this region, which is dominated by the static component. When the prisms are at the other three radial locations, the tornado-like loading is significantly influenced by the aerodynamically induced pressure in addition to the static pressure. For the four radial locations at which the prisms were tested, the magnitude of the mean tornado-like loading is often the largest when the prisms are at the core radius location but the fluctuation of the loading is the most intensive when the prisms are at locations further inside the vortex due to the intensification of the fluctuations of both the static pressure and the velocity of the flow. In addition, while the pressures acting on the prisms mostly exhibits characteristics of Gaussian distribution when the prisms are two core radii from the axis of the vortex, the pressures can be highly non-Gaussian when the prisms are at or inside the core radius of the vortex because both the velocity of the flow and the fluctuation of the static pressure in those regions can be highly non-Gaussian. However, it is observed that when the prisms are at or inside the core radius of the vortex, the characteristics of the resultant forces deviate much less significantly from those of the Gaussian distribution than do the pressures acting over certain areas of the faces of the prisms.

The data also Indicate that the clearance ratio of the prisms can significantly affect the tornado-like loading. In particular, it is observed that the vertical component of the force acting on the prisms depend critically on whether the prisms are elevated or unelevated. When the prism is elevated, both the mean value and the standard deviation of the vertical component of the force are small due to the offset of the pressures acting on the top and bottom faces; when the prism is unelevated, both the mean value and the standard deviation of the vertical component of the force are much larger because, in this case, there is no flow-induced pressure acting on the bottom face. By contrast, the effect of the clearance ratio on the horizontal component of the force is much less significant.

Lastly, the data suggest that for the four radial locations at which the prisms were tested the effect of the depth to height ratio of the prism is the most significant at the core radius location. This is because the depth to height ratio influences the aerodynamically induced pressure by affecting the separation of the flow from the prism and the relative contribution of the aerodynamically induced pressures to the total loading is the most significant when the prism is at this radial location.

In addition to revealing the characteristics of the tornado-like loading on the rectangular prisms, the study also produces a complete dataset in terms of the first four statistical moments of the pressures and resultant forces acting on the prisms. This dataset can serve as a benchmark against which results from other experimental and numerical studies of tornado-like loading on similar generic shapes can be compared to or validated.

Declaration of competing interest

The authors declare that they have no known competing financial interests or personal relationships that could have appeared to influence the work reported in this paper.

Acknowledgments

The measurements of the loading on the prism with a unit depth to height ratio were conducted as a part of the Joint Research initiated in 2016 by Texas Tech University (TTU), USA and Central Research Institute of Electric Power Industry (CRIEPI), Japan. The authors at Texas Tech University acknowledge partial support for the rest of the study from the National Science Foundation under award number CMMI 1763109.

References

Bluestein, H.B., Weiss, C.C., French, M.M., Holthaus, E.M., Tanamachi, R.L., Frasier, S., Pazmany, A.L., 2007. The structure of tornadoes near Attica, Kansas, on 12 2004: High-resolution, mobile, Doppler radar observations. Mon. Weather Rev. 135, 475–506.

Cao, S., Wang, J., Cao, J., Zhao, L., Chen, X., 2015. Experimental study of wind pressures acting on a cooling tower exposed to stationary tornado-like vortices. J. Wind Eng. Ind. Aerodyn. 145, 75–86.

Church, C.R., Snow, J.T., Baker, G.L., Agee, E.M., 1979. Characteristics of tornado-like vortices as a function of swirl ratio: A laboratory investigation. J. Atmos. Sci. 36, 1755–1776.

Gairola, A., Bitsuamlak, G., 2019. Numerical tornado modeling for common interpretation of experimental simulators. J. Wind Eng. Ind. Aerodyn. 186, 32–48.

Gurley, K., Kareem, A., 1997. Analysis interpretation modeling and simulation of unsteady wind and pressure data. J. Wind Eng. Ind. Aerodyn. 69–71, 657–669.

Haan, F.L., Balaramudu, Jr., V., Sarkar, P.P., 2010. Tornado-induced wind loads on a low-rise building. J. Struct. Eng. 136, 106–116.

Haan, F.L., Sarkar, Jr., P.P., Gallus, W.A., 2008. Design, construction and performance of a large tornado simulator for wind engineering applications. Eng. Struct. 30, 1146–1159.

Holmes, J.D., 1979. Mean and fluctuating internal pressure induced by wind. In: Fifth International Conference on Wind Engineering, Fort Collins, Co, USA. pp. 435–450.

Houser, J.L., Bluestein, H.B., Snyder, J.C., 2015. Rapid-scan, polarimetric, Doppler radar observations of tornadogenesis and tornado dissipation in a tornadic supercell: The El Reno, Oklahoma storm of 24 2011. Mon. Weather Rev. 143, 2685–2710.

Jischke, M., Light, B., 1984. Laboratory simulation of tornadic wind loads on a rectangular model structure. In: Wind Engineering, Vol. 1983, Part 3A.. Elsevier, pp. 371–382.

Karstens, C.D., Samaras, T.M., Lee, B.D., Gallus, W.A., Finley, C.A., 2010. Near-ground pressure and wind measurements in tornadoes. Mon. Weather Rev. 138, 2570–2588.

Kopp, G.A., Oh, J.H., Inculet, D.R., 2008. Wind-induced internal pressures in houses. J. Struct. Eng. 134, 1129–1138.

Kopp, G.A., Wu, C.-H., 2020. A framework to compare wind loads on low-rise buildings in tornadoes and atmospheric boundary layers. J. Wind Eng. Ind. Aerodyn. 204, 104269.

Kosiba, K., Wurman, J., 2010. The three-dimensional axisymmetric wind field structure of the spencer, South Dakota, 1998 tornado. J. Atmos. Sci. 67, 3074–3083.

Kosiba, K.A., Wurman, J., 2013. The three-dimensional structure and evolution of a tornado boundary layer. Weather Forecast. 28, 1552–1561.

Letchford, C.W., 2001. Wind loads on rectangular signboards and hoardings. J. Wind Eng. Ind. Aerodyn. 89, 135–151.

Letchford, C., Levitz, B., James, D., 2015. Internal Pressure Dynamics in Simulated Tornadoes, Structures Congress 2015. American Society of Civil Engineers, pp. 2689–2701.

Liu, Z., Ishihara, T., 2015. Numerical study of turbulent flow fields and the similarity of tornado vortices using large-eddy simulations. J. Wind Eng. Ind. Aerodyn. 145, 42–60.

Liu, Z., Zhang, C., Ishihara, T., 2018. Numerical study of the wind loads on a cooling tower by a stationary tornado-like vortex through LES. J. Fluids Struct. 81, 656–672.

Lombardo, F.T., Roueche, D.B., Prevatt, D.O., 2015. Comparison of two methods of near-surface wind speed estimation in the 22 May, 2011 Joplin, Missouri tornado. J. Wind Eng. Ind. Aerodyn. 138, 87–97.

Mishra, A.R., James, D.L., Letchford, C.W., 2008. Physical simulation of a single-celled tornado-like vortex, Part B: Wind loading on a cubical model. J. Wind Eng. Ind. Aerodyn. 96, 1258–1273.

Natarajan, D., Hangan, H., 2012. Large eddy simulations of translation and surface roughness effects on tornado-like vortices. J. Wind Eng. Ind. Aerodyn. 104–106, 577–584.

Pauley, R.L., Church, C.R., Snow, J.T., 1982. Measurements of maximum surface pressure deficits in modeled atmospheric vortices. J. Atmos. Sci. 39, 369–377.

Rajasekharan, S.G., Matsui, M., Tamura, Y., 2013. Characteristics of internal pressures and net local roof wind forces on a building exposed to a tornado-like vortex. J. Wind Eng. Ind. Aerodyn. 112, 52–57.

Refan, M., Hangan, H., 2018. Near surface experimental exploration of tornado vortices. J. Wind Eng. Ind. Aerodyn. 175, 120–135.

Roueche, D.B., Prevatt, D.O., Haan, F.L., 2020. Tornado-induced and straight-line wind loads on a low-rise building with consideration of internal pressure. Front. Built Environ. 6.

Sabareesh, G.R., Matsui, M., Tamura, Y., 2012. Dependence of surface pressures on a cubic building in tornado like flow on building location and ground roughness. J. Wind Eng. Ind. Aerodyn. 103, 50–59.

Sabareesh, G.R., Matsui, M., Tamura, Y., 2013. Ground roughness effects on internal pressure characteristics for buildings exposed to tornado-like flow. J. Wind Eng. Ind. Aerodyn. 122, 113–117.

Selvam, R.P., Millet, P.C., 2003. Computer modeling of tornado forces on buildings. Wind Struct. 6, 209–220.

Selvam, R.P., Millet, P.C., 2005. Large eddy simulation of the tornado–structure interaction to determine structural loadings. Wind Struct. 8, 49–60.

Smith, D.A., Zuo, D., Mehta, K.C., 2014. Characteristics of wind induced net force and torque on a rectangular sign measured in the field. J. Wind Eng. Ind. Aerodyn. 133, 80–91.

Tang, Z., Feng, C., Wu, L., Zuo, D., James, D.L., 2018a. Characteristics of tornado-like vortices simulated in a large-scale ward-type simulator. Bound.-Lay. Meteorol. 166, 327–350.

Tang, Z., Zuo, D., James, D., Eguchi, Y., Hattori, Y., 2018b. Effects of aspect ratio on laboratory simulation of tornado-like vortices. Wind Struct. 27, 111–121.

Thampi, H., Dayal, V., Sarkar, P.P., 2011. Finite element analysis of interaction of tornados with a low-rise timber building. J. Wind Eng. Ind. Aerodyn. 99, 369–377.

Wang, J., Cao, S., Pang, W., Cao, J., 2017. Experimental study on effects of ground roughness on flow characteristics of tornado-like vortices. Bound.-Lay. Meteorol. 162, 319–339.

Zuo, D., Smith, D.A., Mehta, K.C., 2014. Experimental study of wind loading of rectangular sign structures. J. Wind Eng. Ind. Aerodyn. 130, 62–74.